

Timing resolution from very thin LGAD sensors tested on particle beam down to 12 ps

Robert Stephen White^a, Marco Ferrero^a, Valentina Sola^{b,a}, Anna Rita Altamura^{b,a}, Roberta Arcidiacono^{c,a}, Maurizio Boscardin^{d,e}, Nicolò Cartiglia^a, Matteo Centis Vignal^{d,e}, Tommaso Croci^f, Matteo Durando^b, Simone Galletto^b, Alessandro Fondacci^f, Leonardo Lanteri^{b,a}, Ludovico Massaccesi^{b,a}, Luca Menzio^{c,a}, Arianna Morozzi^f, Francesco Moscatelli^{g,f}, Daniele Passeri^{h,f}, Giovanni Paternoster^{d,e}, Federico Siviero^a

^a*Istituto Nazionale di Fisica Nucleare, Sezione di Torino, via P. Giuria 1, Torino, Italy*

^b*Università degli Studi di Torino, via P. Giuria 1, Torino, Italy*

^c*Università del Piemonte Orientale, largo Donegani 2, Novara, Italy*

^d*Fondazione Bruno Kessler, via Sommarive 18, Povo, Trento, Italy*

^e*Trento Institute for Fundamental Physics and Applications, via Sommarive 14, Povo, Trento, Italy*

^f*Istituto Nazionale di Fisica Nucleare, Sezione di Perugia, via A. Pascoli, Perugia, Italy*

^g*Consiglio Nazionale delle Ricerche, Istituto Officina dei Materiali, via A. Pascoli, Perugia, Italy*

^h*Università degli Studi di Perugia, via G. Duranti 93, Perugia, Italy*

Abstract

The paper reports on the timing resolution achieved with Low-Gain Avalanche Diode (LGAD) sensors optimised for very-high fluences at the DESY Test Beam Facility using 4 GeV/c electrons. The LGADs adopt an *n*-in-*p* technology with a *p*⁺-type boron gain implant, co-implanted with carbon to mitigate acceptor deactivation. The substrate thickness of the sensors varies from 20 μm to 45 μm , with an active area spanning from 0.75×0.75 to $1.28 \times 1.28 \text{ mm}^2$. A set of 30 μm sensors irradiated with neutrons at fluences between 0.4×10^{15} and $2.5 \times 10^{15} \text{ n}_1 \text{ MeV eq.cm}^{-2}$ were tested on the beam. The gain was measured between 7 and 40 across all non-irradiated sensors in the study, and between 7 and 30 in irradiated sensors. The experimental setup consisted of a 45 μm -thick trigger sensor with an active area of $3.6 \times 3.6 \text{ mm}^2$, four device-under-test (DUT) planes, and a Photonis micro-channel plate photomultiplier tube (MCP) as a time reference. The timing resolution was calculated from Gaussian fitting of the difference in times of

arrival of a particle at the DUT and the MCP, using the constant fraction discrimination technique. A timing resolution of 26.4 ps was achieved in 45 μm sensors, and down to 16.6 ps in 20 μm sensors. The combination of two 20 μm LGAD sensors reached a timing resolution of 12.2 ps. A timing resolution of 20 ps was obtained in all irradiated 30 μm sensors.

Keywords: Solid State Radiation Sensors; Thin LGAD Sensors; Radiation Hardness; Precision Timing

1. Introduction

Future High-Energy Physics (HEP) experiments are expected to reach significantly higher instantaneous luminosities and, therefore, will require detectors capable of operating under extreme-fluence conditions. In the CERN High-Luminosity Large Hadron Collider (HL-LHC), the innermost tracking layers of the high energy detectors, A Toroidal LHC Apparatus (ATLAS) and Compact Muon Solenoid (CMS), will be exposed to a fluence of $3.5 \times 10^{16} \text{ n}_1 \text{ MeV eq.cm}^{-2}$ [1, 2], while in the Future Circular Collider (FCC-hh), this is expected to reach $\sim 6 \times 10^{16} \text{ n}_1 \text{ MeV eq.cm}^{-2}$ during proton-proton collisions [3, 4].

Low-Gain Avalanche Photodiode (LGAD) technology is at the forefront of future detectors, due to its superior timing resolution and radiation hardness [5]. Current LGAD technology can achieve a temporal resolution between 25 and 35 ps depending on substrate thickness (sub-55 μm) [6], and can survive in high radiation environments up to $\sim 2 \times 10^{15} \text{ n}_1 \text{ MeV eq.cm}^{-2}$ while returning a modest gain [7].

The LGAD sensors used in the analysis have been designed to investigate how thin substrates respond to irradiation to the extreme fluences (EXFLU), and how timing resolution and gain, among other properties, evolve with substrate thickness and irradiation fluence. Two batches of sensors manufactured by the Fondazione Bruno Kessler (FBK) were employed. The EXFLU0 sensors have the same layout and gain implant design as the UFSD3.2 sensor produced at FBK, but on thinner substrates, namely 25 and 35 μm . While EXFLU1 sensors have a dedicated sensor layout, with optimised peripheral structures, and further explore the beneficial effects derived from thin substrates, down to 15 μm . The sensors were irradiated with neutrons in the TRIGA Mark II research nuclear reactor at the Jozef Stefan Institute [8]. The characterisation and performance of EXFLU sensors, both before and

after irradiation, were completed at the laboratory in Turin, and are reported in [9, 10, 11, 12].

This paper reports on the performance of the EXFLU sensors at the Test Beam Facility at DESY [13]. The EXFLU design is described in detail in Section 2. The experimental setup and the approaches to data acquisition (DAQ) and signal analysis are explained in Section 3. The timing resolution measurements are presented for both non-irradiated and irradiated samples in Section 4. Conclusions on the timing performance of the EXFLU sensors are drawn in Section 5.

2. The EXFLU LGAD Design

The LGAD design comprises of a silicon pixel sensor with a substrate active thickness of tens of microns (usually $\sim 50 \mu\text{m}$), implanted with a gain layer $\sim 1 \mu\text{m}$ beneath the surface, operating with a gain of ~ 20 . In this study, n -in- p LGADs with a p -type high-resistivity bulk are used. The gain implant is boron-doped with a carefully tuned peak p^+ -type concentration of $\sim 10^{16} \text{ cm}^{-3}$ at a depth of $\sim 1 \mu\text{m}$ within the substrate, illustrated in Figure 1. A carbon co-implant is also injected into the gain layer to mitigate the deactivation of boron acceptors due to the effects of irradiation [14, 15].

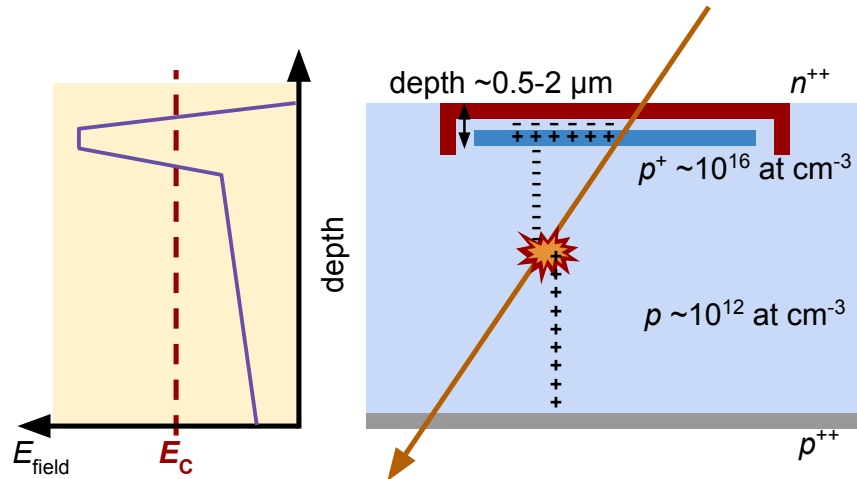


Figure 1: Specifications for the LGAD sensors studied: an n -in- p design with a peak boron (p^+ -type) doping concentration of $\sim 10^{16} \text{ cm}^{-3}$ in the gain implant.

Implantation and thermal activation of the carbon and boron acceptors to synthesise the gain layer adhere to two different schemes: low-carbon, low-boron diffusion (CBL), and high-carbon, low-boron diffusion (CHBL) [16]. The CBL mode involves implanting carbon and boron, followed by simultaneous thermal activation at low temperature. The CHBL mode involves implantation and activation of carbon under a high heat load, followed by implantation and activation of boron at a lower temperature.

The EXFLU0 batch of sensors was implanted under the CHBL mode. A single-pad (SP) device measures $1.28 \times 1.28 \text{ mm}^2$ at the surface, while the dual-pad LGAD-PIN (LP) device measures $1.0 \times 1.0 \text{ mm}^2$ on each pad.

The EXFLU1 batch of sensors differs from the EXFLU0 batch primarily in implantation, geometry, and periphery design. The EXFLU1 sensors were implanted under the CBL mode with the exception of one 20 μm -thick design. The SP geometry is identical across EXFLU batches, whereas the EXFLU1 LP device has a smaller active area, measuring $0.75 \times 0.75 \text{ mm}^2$ per pad. The difference in periphery design results in a slightly lower bulk breakdown voltage on average for EXFLU0 sensors at a given thickness, but produces comparable results for the purposes of the timing study. The EXFLU0 and EXFLU1 schematics for both SP and LP devices are illustrated in Figure 2.

The nominal thicknesses of the sensors studied at the Test Beam Facility range from 20 to 45 μm . The effective active substrate thickness is therefore considered to be the nominal thickness minus 2 μm for the LGADs. Considering the capacitance of each sensor using a parallel-plate approximation, the LP device with a smaller active area was used for sensors with an active thickness less than 35 μm . This ensures that the sensor capacitance is maintained below 5 pF after full sensor depletion.

The p_{bulk} of sensors with thicknesses less than 30 μm is $1.5 \times 10^{14} \text{ cm}^{-3}$; for 30 μm sensors, $1.5 \times 10^{13} \text{ cm}^{-3}$; and for thicknesses greater than 30 μm , it is not possible to measure through capacitance-voltage testing but is expected to be very low.

The design specifications, including the p^+ relative dose (normalised to the FBK reference dose and expressed in arbitrary units), p_{bulk} , the devices tested (DUTs), and the pad capacitance are summarised in Table 1. In all sensors studied, a carbon dose of 1.0 is co-implanted according to [16].

At least one non-irradiated sensor of each thickness was tested at the Test Beam Facility. A single CHBL and CBL device was tested in the case of the 20 μm sensor. EXFLU1 30 μm sensors irradiated to the fluences of 0.4×10^{15} , 0.8×10^{15} , 1.5×10^{15} , and $2.5 \times 10^{15} \text{ n}_{1 \text{ MeV eq}} \text{ cm}^{-2}$ have been

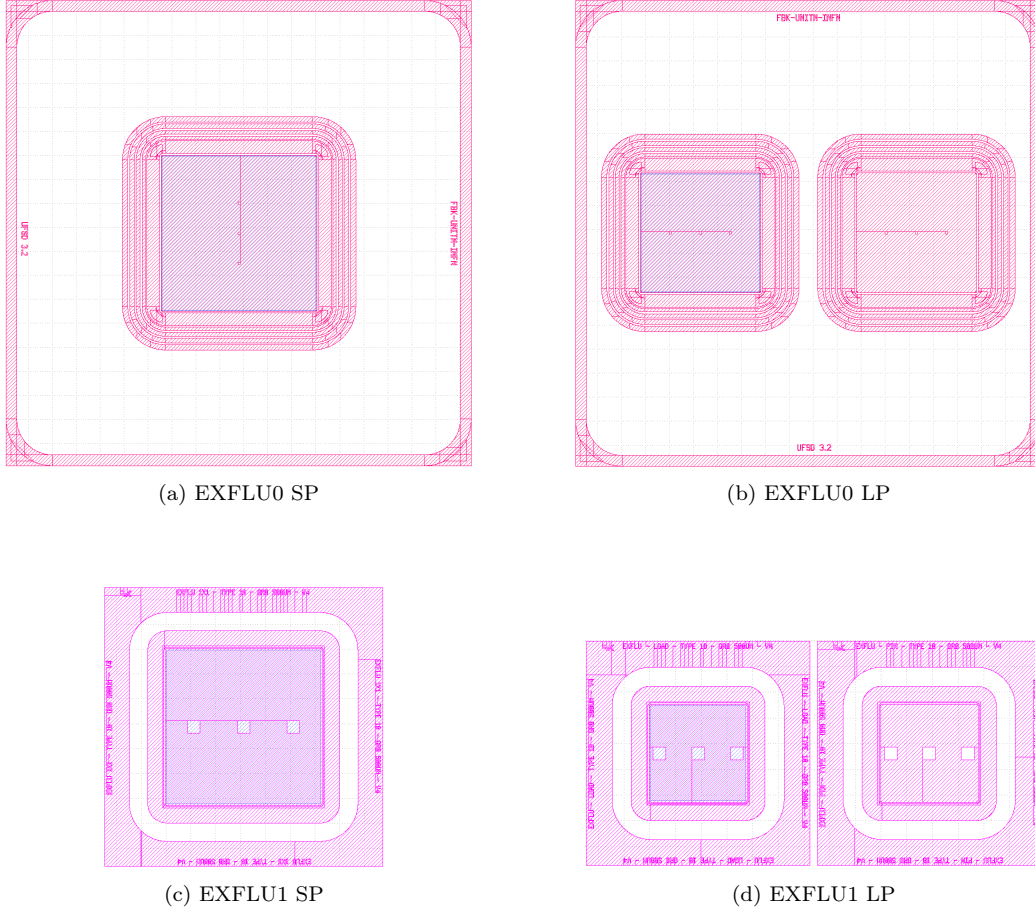


Figure 2: Schematic images of EXFLU SP and LP devices used for timing performance studies, shown to scale: the EXFLU0 SP (a) and LP (b) devices with an active area of $1.28 \times 1.28 \text{ mm}^2$ and $1.0 \times 1.0 \text{ mm}^2$ per pad, respectively, and the EXFLU1 SP (c) and LP (d) devices with an active area of $1.28 \times 1.28 \text{ mm}^2$ and $0.75 \times 0.75 \text{ mm}^2$ per pad, respectively.

Table 1: The design specifications and device types tested, with relative peak gain layer doping concentration, implantation mode, p_{bulk} , device type, and sensor capacitance. The EXFLU0 sensors are demarcated as the 35 and 25 μm substrates, while the EXFLU1 samples correspond to the 45, 30, and 20 μm substrates. The p^+ dose is normalised to the FBK reference value. All sensors have a carbon co-implantation of value 1.0, following [16].

Thick. [μm]	p^+ dose [a.u.]	Diffusion	p_{bulk} [cm^{-3}]	DUT	C_{DUT} [pF]
35	0.94	CHBL	-	SP	4.8
25	0.94	CHBL	1.5×10^{14}	LP	4.1
45	1.14	CBL	-	SP	3.9
30	1.12	CBL	1.5×10^{13}	LP	1.9
20	0.80	CHBL	1.5×10^{14}	LP	2.9
20	0.96	CBL	1.5×10^{14}	LP	2.9

tested on beam. All measurements on the irradiated sensors were performed after annealing at 60°C for 80 minutes [17].

The EXFLU1 sensors are well established as having the best acceptor-removal mitigation performance of any thin LGAD produced by FBK to date [11, 12]. The irradiated sensors used for this study have demonstrated that the gain performance observed in the non-irradiated sensors can be reproduced up to a fluence of 2.5×10^{15} n₁ MeV_{eq}.cm⁻² when operated at a sufficiently high bias [14].

2.1. Timing resolution in LGADs

In the context of timing performance, the dominant contributions to the resolution in thin LGADs are the electronic noise, or jitter, which affects the shape of the signal, and the non-uniform energy deposition by ionising particles traversing the sensors [16].

The timing resolution σ_t is therefore given by:

$$\sigma_t^2 = \sigma_{\text{jitter}}^2 + \sigma_{\text{ionisation}}^2 , \quad (1)$$

where σ_{jitter} and $\sigma_{\text{ionisation}}$ are the jitter and ionisation contributions, respectively.

The jitter is intrinsically related to the electronics readout noise and bandwidth under the relation:

$$\sigma_{\text{jitter}} = \frac{N}{\frac{dV}{dt}} \approx \frac{t_{\text{rise}}}{\frac{S}{N}} , \quad (2)$$

where N is the noise, taken as the root-mean-square (RMS) noise of the signal baseline, $\frac{dV}{dt}$ is the slew rate of the oscilloscope, and S and t_{rise} are the signal magnitude and rise time, respectively. A smaller electronics bandwidth yields lower noise, whereas a higher slew rate, which minimises jitter, requires a larger bandwidth. Equation 2 implies that t_{rise} is directly proportional to σ_{jitter} , and therefore, given that faster signals are produced in thinner sensors, σ_t is smaller.

The contribution $\sigma_{\text{ionisation}}$ is invariant of the collected charge but is lower for thinner sensors, given that the faster signals are less sensitive to fluctuations in the signal. The value for $\sigma_{\text{ionisation}}$ can be estimated using a fit between the σ_t (DUT) and charge values for each DUT using the formula:

$$\sigma_t^2 = a^2 + \left(\frac{b}{Q}\right)^2, \quad (3)$$

where Q is the charge, and a and b are constants terms [18]. In this case, a corresponds to the $\sigma_{\text{ionisation}}$ term and is fixed for a given device.

3. EXFLU operations at the DESY Test Beam Facility

Each sensor sample was read out using a single-channel Santa Cruz (SC) board configured with a 470Ω inverting transimpedance amplifier integrated with an Infineon SiGe RF transistor, capable of supporting bandwidths of $\mathcal{O}(10 \text{ GHz})$ while providing low noise and high gain [16]. An external amplification stage is incorporated using a commercial low-noise Cividic C1 broadband amplifier with 2 GHz bandwidth and 20 dB gain. The DAQ was performed using an eight-channel Lecroy WaveRunner 8208HD oscilloscope, with a 10 GSa/s sampling rate and 2 GHz bandwidth. The overall system bandwidth, BW_{tot} , is $\sim 1.4 \text{ GHz}$, corresponding to a limit on the measurable inverted signal $t_{\text{rise}} = 0.35/BW_{\text{tot}}$ of 250 ps. The sensors selected for the timing study are not limited by the bandwidth, nor is the minimum measurable t_{rise} reached for the thinnest sensor substrates, expected to be between 300 and 350 ps (see Section 4).

The electron beam momentum at the Test Beam Facility was set to 4 GeV/c, resulting in a particle flux of 1.0 kHz/cm^2 . The flux is recorded at the facility's beam monitor and may underestimate the effective rate.

Two different apparatuses were used, one for non-irradiated DUTs and the other for irradiated ones. The former operates at ambient temperature, which for the Test Beam Facility was constantly at 18°C during the testing

campaign. The latter uses a polythene cold box filled with solidified CO₂ to maintain an operating temperature as low as -50°C, monitored using a DHT11 temperature and humidity sensor integrated with an Arduino system.

Each apparatus is set up with a series of three parallel SC boards mounted with sensors for DAQ, in the following order of beam incidence: a 45 μm trigger sensor with active area $3.6 \times 3.6 \text{ mm}^2$, operated at 230 V in the non-irradiated DUT setup and at 140 V in the irradiated DUT setup, taking into account the different temperature of operation, with a minimum inverted signal threshold of 40 mV; the first DUT, DUT 1; the second DUT, DUT 2, of the same thickness as DUT 1; and a Photonis micro-channel plate photomultiplier tube (MCP) used as a timing reference. The DUTs were read out simultaneously with the trigger and MCP during data acquisition for each run. The intrinsic timing resolution of the MCP was calculated at $5 \pm 2 \text{ ps}$ using the data taken with 20 μm sensors, as outlined in Section 3.2.

For each DUT bias point, a DAQ stopping condition of at least 30,000 trigger events was required, equal to about 40 minutes of data taking. The coincidence rate between the trigger sensor and MCP yielded a 97% geometric efficiency, and between the DUTs and MCP from 3.4 to 12.7% coincidence, depending on the sensor geometry. Across all bias points for a given DUT, DAQ was performed for up to 8 hours continuously. A temperature variation of -50 to -42°C was recorded by the DHT11 Arduino sensor with the exception of the sample irradiated at $1.5 \times 10^{15} \text{ n}_1 \text{ MeV eq.cm}^{-2}$, which was measured from -50 to -35°C. The variation in temperature is due to the reduction in CO₂ volume caused by sublimation during data taking.

The operating conditions of EXFLU sensors are suited for timing performance analysis. The reverse bias corresponding to bulk breakdown due to gain in each sample lies within a range of 100 V and 250 V, as shown in Figure 3. The range of bias points applied to the DUTs during data taking is selected at varying intervals from a bulk electric-field strength of at least $3 \text{ V}\mu\text{m}^{-1}$ to the DUT breakdown. The lower bias threshold corresponds to the point at which the electron drift velocity is saturated. This ensures a clear separation between the amplitudes of signal and noise events, as demonstrated in Figure 4 for the CBL-activated 20 μm device operated at 150 V bias at 18°C. In this example, the region of signal events lies above an amplitude of 25 mV. The shape of this distribution is typical of the data collected for almost all EXFLU samples: the noise peak width is mostly constant until near the sensor breakdown, while the distribution of signal events broadens, with a higher average amplitude and a more pronounced separation from

noise events under higher biases. The noise in the 45 μm samples were much larger than in other samples during DAQ. Thus, for better comparison with the other thicknesses, the 45 μm results are replaced with low-noise data obtained using a 45 μm sensor tested with a ^{90}Sr β source with an activity of 37 kBq at 18°C. Most recorded events come from end-point β electrons with an energy of 2.28 MeV and can be treated as MIP-like. A single-plane setup is used, with the MCP as the trigger and timing reference, due to the significantly lower energy and flux of ionising particles emitted by the β source.

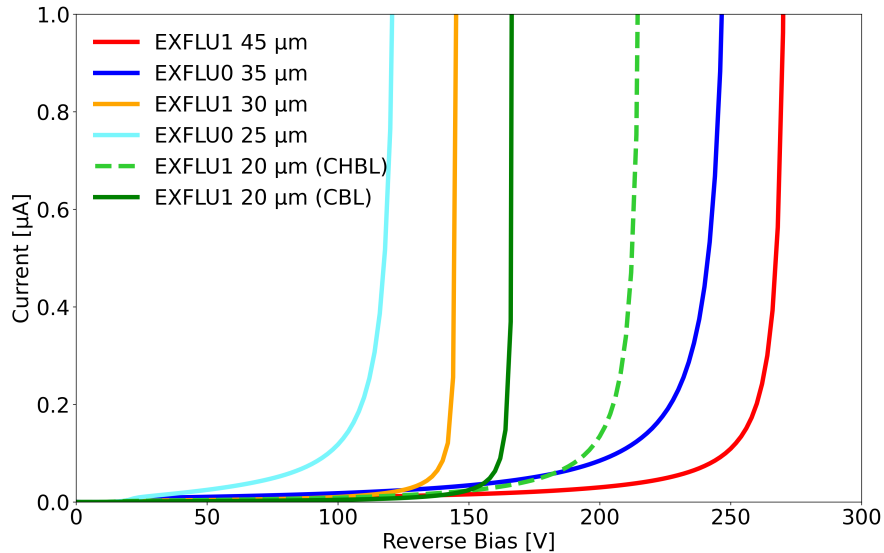


Figure 3: The breakdown trends for the non-irradiated EXFLU samples. The two 20 μm EXFLU1 sensors differ in the gain-implantation method, with the CHBL-activated sensors exhibiting a higher breakdown voltage.

The breakdown trends for irradiated sensors are obtained from measuring the leakage current as a function of the reverse bias at -20°C. Operating sensors at low temperatures is necessary to mitigate the increase in leakage current induced by irradiation and to prevent early breakdown. The irradiated 30 μm sensors operate at higher biases than the non-irradiated sample, between 200 and 400 V. The breakdown point of each sensor increases with the level of irradiation, highlighted in Figure 5. The single-event burnout (SEB) limit for a 30 μm -thick substrate is 405 V, considering a maximum electric-field strength of 13.5 $\text{V}\mu\text{m}^{-1}$ [19]. The acceptor removal coefficient in 30 μm

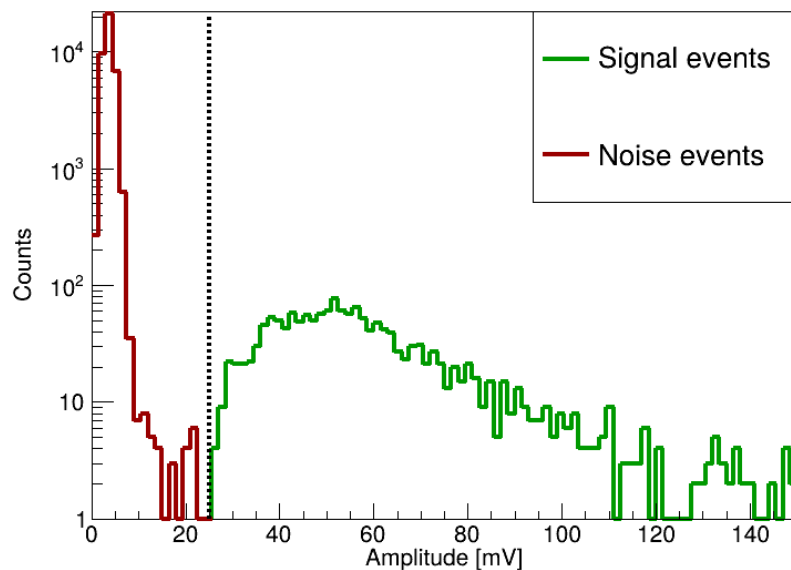


Figure 4: The distribution of signal amplitudes for the 20 μm CBL LGAD sensor operated at 150 V reverse bias and at 18°C, with the selected signal events indicated above amplitudes of 25 mV. The shape of the signal events, following a Landau distribution convoluted with a Gaussian, is typical for all samples.

EXFLU1 sensors was estimated at $1.22 \pm 0.10 \times 10^{-16} \text{ cm}^2 \text{n}_1^{-1} \text{ MeV}_{\text{eq}}$ [12], and is the most radiation-hard gain implant design produced by FBK to date.

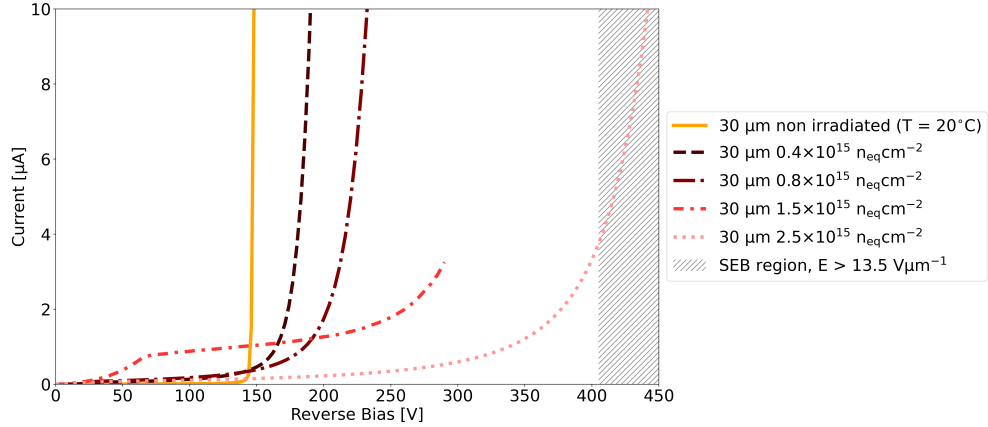


Figure 5: The breakdown curves for the irradiated 30 μm samples, performed at -20°C , highlighting the increasing breakdown with higher fluences due to the onset of acceptor removal. The SEB region is also shown here, above the 405 V threshold for 30 μm sensors [19].

3.1. Signal analysis

The charge injected within the sensor is calculated from the fit of a Landau-plus-Gaussian convolution to the distribution of signal area. The conversion from signal area (in pWb or $\text{mV}\cdot\text{ns}$) to charge (in fC) is given by:

$$Q = \frac{\mathcal{A}}{G_A R_{\text{in}}} , \quad (4)$$

where Q is the charge, \mathcal{A} is the signal area, G_A is the gain amplification factor 10 of the 20 dB Cividec broadband amplifier in the readout chain, and R_{in} is the input impedance of 470Ω for electronic readout with the SC board. The typical charge measured in the non-irradiated samples increases with sensor thickness, ranging from 2 to 8 fC for sensors thinner than 30 μm , increasing up to 10 fC for the 30 μm sensors, and reaching 15 fC for the 35 μm sensors, as shown in Figure 6. The signal gain is calculated from the charge Q using the formula:

$$\text{Gain} = 100 \frac{Q}{d_{\text{eff}}} , \quad (5)$$

where d_{eff} is the effective active substrate thickness. This method is equivalent to computing the fraction of charge collected in the LGAD and in a PIN with identical substrate thickness and area, but without the gain implant, as outlined in [20]. The gain is observed to vary between 7 and 60 across the EXFLU samples, as presented in Figure 7. The resulting signal amplitude at a given gain is observed to be largely invariant of substrate thickness, despite the dependence of thickness on the collected charge. This is in agreement with the Ramo-Shockley theorem [21] assuming a parallel-plate geometry, indicating that the observed differences in charge between the sensors correspond to differences in the signal rise time and duration, and hence are dependent on the thickness, while the maximum signal amplitude that is produced by the gain mechanism is only dependent on the gain and not the substrate thickness. A further consequence is that thinner sensors with higher multiplication will yield better timing resolution.

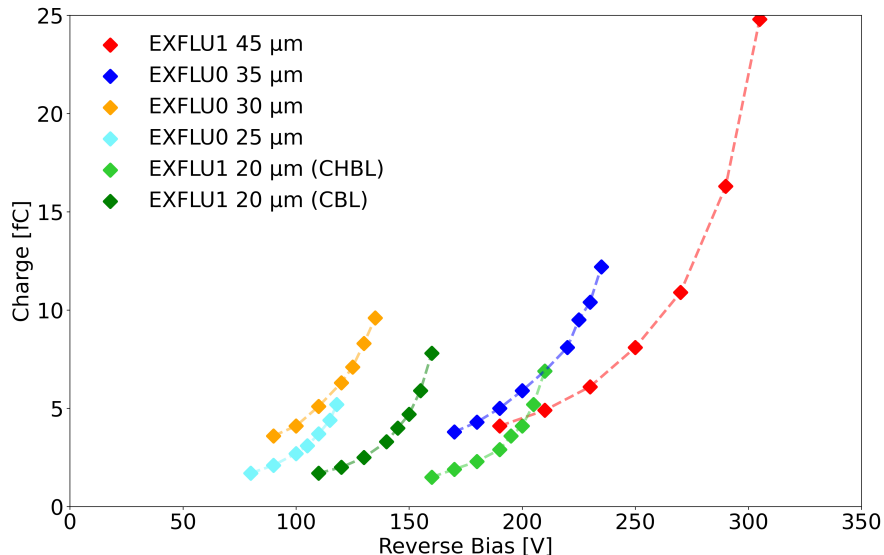


Figure 6: Charge injected into non-irradiated EXFLU samples as a function of the reverse bias, recorded at 18°C, ranging within 2 and 15 fC conditionally on thickness.

The gain measured at a given reverse-bias value in the irradiated 30 μm sensors, using Equation 5, is sensitive to temperature changes during data taking. Therefore, the gain values are shifted by incrementing the effective reverse bias by 2 V per 1°C to obtain a bias range at a fixed temperature

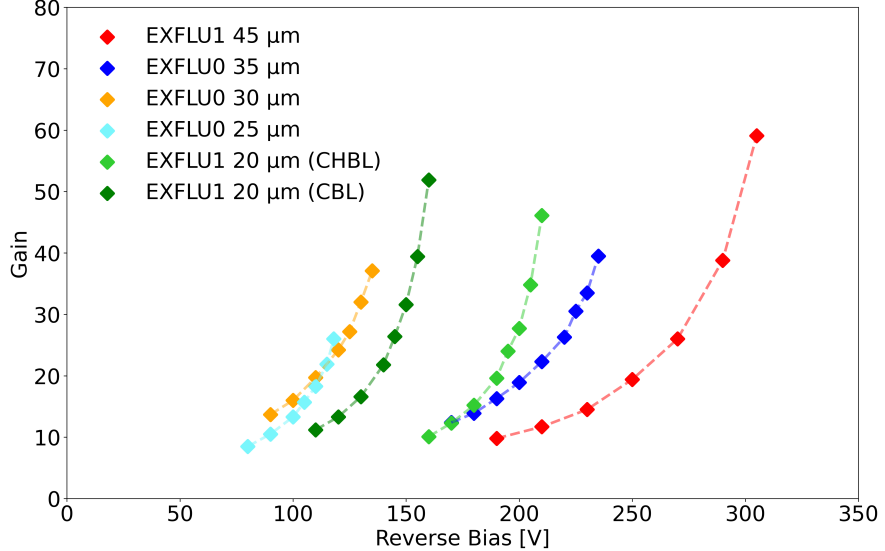


Figure 7: Gain measured in non-irradiated EXFLU samples as a function of the reverse bias, recorded at 18°C, ranging from 7 to 60 largely independent of thickness.

of -42°C [16], corresponding to the highest common temperature of all the irradiated sensors. The temperature correction is small and does not affect the physical quantities of the sensor.

The collected charge varies from 2 to 9 fC in sensors irradiated up to $1.5 \times 10^{15} \text{ n}_1 \text{ MeV eq.cm}^{-2}$, and between 2 and 4.5 fC in the sensor irradiated at $2.5 \times 10^{15} \text{ n}_1 \text{ MeV eq.cm}^{-2}$ at biases below the SEB limit. These correspond to a gain of between 10 and 35, and between 10 and 15, respectively, as demonstrated in Figure 8 for charge values at the temperature the data was recorded, and in Figure 9 for data corrected to -42°C.

The t_{rise} of thin non-irradiated LGADs above the saturation threshold for electron drift velocity of $3 \text{ V}\mu\text{m}^{-1}$, taken at the 10%-90% interval, is observed to decrease from 600 to 300 ps linearly with the sensor thickness. This linear dependence is illustrated in Figure 10, and corresponds to an improving timing resolution in thinner sensors through the σ_{jitter} contribution following the discussion in Section 2.1. The noise is quantified as the signal baseline RMS and is mainly due to the electronics in the setup. The RMS noise remains stable under increasing reverse bias until sensor breakdown, at which point an increase is observed. In the 45 μm sensor, the RMS noise is

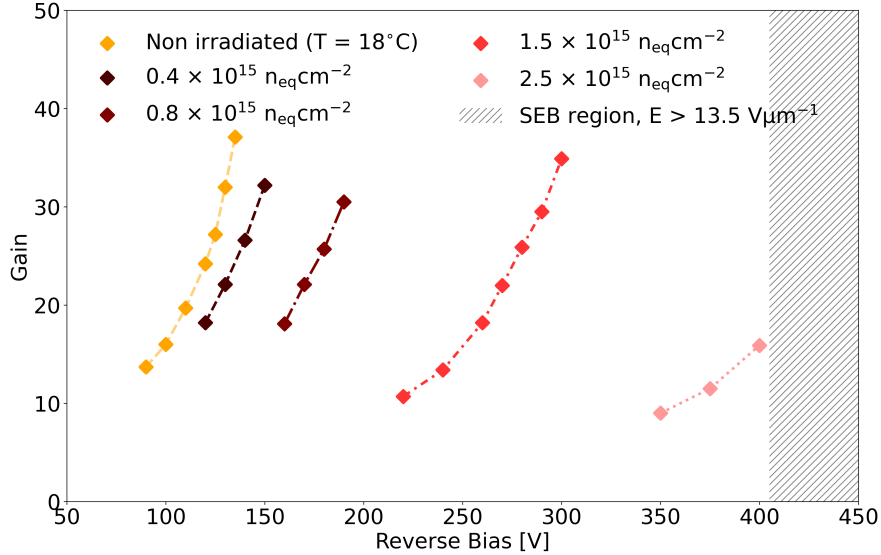


Figure 8: Gain measured in the 30 μm EXFLU samples as a function of the reverse bias, recorded at 18°C for the non-irradiated sample and between -50 and -35°C in the irradiated samples. The signal multiplication ranges from 10 to 35.

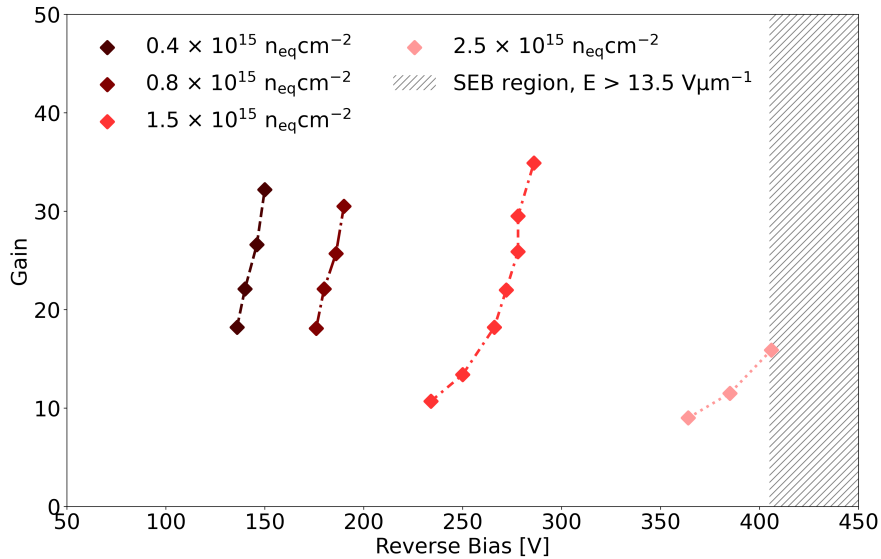


Figure 9: Gain measured in the irradiated 30 μm EXFLU samples as a function of the reverse bias, corrected to -42°C. The signal multiplication ranges from 10 to 35.

around 1.8 mV, ranges from 1.3 to 1.5 mV in the 25, 30, and 35 μm sensors, and is between 1.4 and 1.6 mV in 20 μm samples.

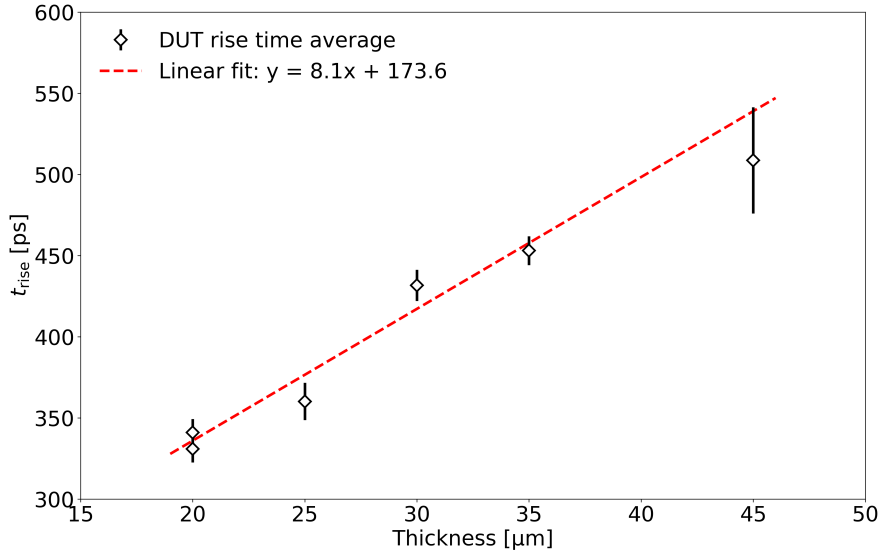


Figure 10: The t_{rise} of each non-irradiated EXFLU sample, taken at the 10%-90% interval, demonstrating a linear relationship with the thickness of the sensor.

The t_{rise} decreases marginally with fluence in the irradiated 30 μm samples, due to the increased bulk electric-field strength. The RMS noise in these samples ranges from 1.2 to 1.4 mV, except for the sample irradiated at $1.5 \times 10^{15} \text{ n}_1 \text{ MeV eq.cm}^{-2}$, which reached 2.2 mV at breakdown.

The timing resolution is calculated from coincident DUT and MCP events that pass the signal selection and are processed with a constant fraction discriminator (CFD). In addition to the DUT signal event selection described by Figure 4, a selection is applied to MCP events. This requires MCP events with amplitudes above the threshold of 40 mV but below the oscilloscope vertical scale saturation, set to 540 mV. The sensitivity of the timing resolution to additional event selections was found to be negligible. The optimal CFD thresholds were found to correspond to the time-of-arrival at the 30% level for all tested sensors. The distribution of the difference in CFD values from the DUT and MCP events is then fitted with a Gaussian formula, and the standard deviation of the fit is the timing resolution of the combined DUT-MCP system, $\sigma_t(\text{DUT}; \text{MCP})$. The timing resolution of the DUT, $\sigma_t(\text{DUT})$,

is calculated from the quadrature difference:

$$\sigma_t(\text{DUT}) = \sqrt{\sigma_t^2(\text{DUT}; \text{MCP}) - \sigma_t^2(\text{MCP})} , \quad (6)$$

where $\sigma_t(\text{MCP})$ is the contribution due to the intrinsic timing resolution of the MCP. A $\sigma_t(\text{MCP})$ value of 5 ± 2 ps is extracted using the two non-irradiated 20 μm sensors, as outlined in Section 3.2.

The statistical uncertainty on $\sigma_t(\text{DUT})$ calculated directly from the Gaussian fitting is $\lesssim 2\%$. The number of selected signal events in the calculation of $\sigma_t(\text{DUT})$, both for LP and SP devices, is sufficient that the statistical contribution is negligible in the overall uncertainty.

The most significant sources of uncertainty in the timing resolution measurement are systematic in nature, described by Equation 1 [16]. The σ_{jitter} contribution, measured using the approximation in Equation 2, is $\lesssim 10$ ps in sensors below 45 μm and $\lesssim 20$ ps in the 45 μm sample, shown in Figure 11. The $\sigma_{\text{ionisation}}$ term is measured with the fit described in Equation 3, and is observed to decrease from 25 ps for the 45 μm sample to 15 ps in the 20 μm samples, shown in Figure 12. The results are corroborated by previous measurements of sensors with thicknesses ranging from 35 μm to 80 μm using the β setup [18], and are in good agreement with the predicted $\sigma_{\text{ionisation}}$ trend from Weightfield2 simulations [22]. This is in agreement with the expectation that thinner sensors, which produce signals with a steeper rising edge, are less affected by fluctuations from non-uniform ionisation of traversing particles within the sensor.

Another significant systematic uncertainty is from the $\sigma_t(\text{MCP})$ measurement. The 2 ps uncertainty is a precise practical estimate using the samples available, given the low $\sigma_t(\text{MCP})$ of 5 ps. The uncertainties on the $\sigma_t(\text{DUT})$ estimates are nonetheless minimal, between 0.5 and 1.1 ps for the non-irradiated samples, and between 0.7 and 0.8 ps for the irradiated samples. The 45 μm sample tested at the β setup has an uncertainty range of 0.8 to 1.5 ps.

A study was performed to estimate the systematic uncertainty in determining the signal amplitude due to the sampling rate of the oscilloscope, which directly affects the CFD. A large subset of signal data with amplitude within a 1 mV range was used. The functional form used to extract the amplitude was compared across different distributions, such as symmetric Gaussian, Lorentzian, parabolic, and Voigtian fits, and asymmetric Landau and skewed-Gaussian fits. The effect was found to be negligible on the over-

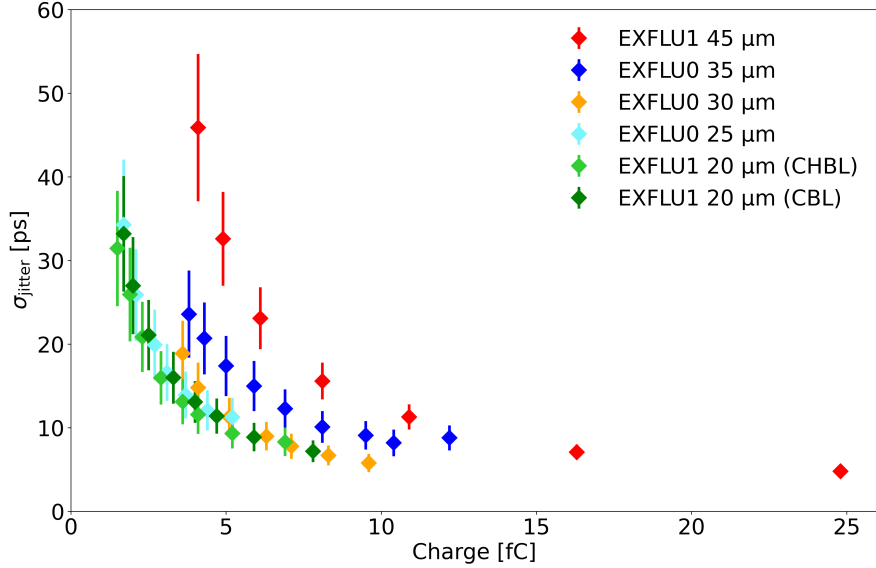


Figure 11: The σ_{jitter} contribution as a function of charge collected by EXFLU samples. A sub-10 ps σ_{jitter} is achieved in all sensors of thickness below 45 μm .

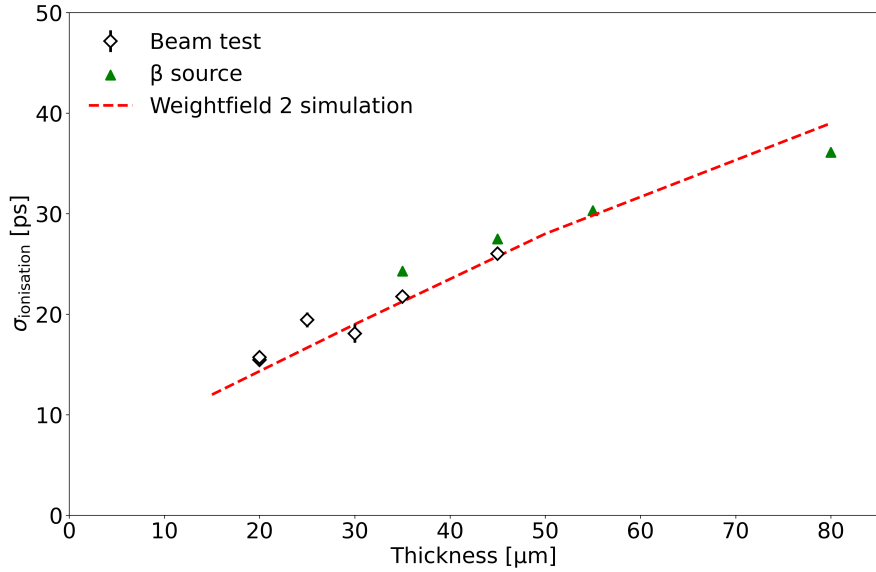


Figure 12: The $\sigma_{\text{ionisation}}$ contribution as a function of thickness using test beam data and from samples measured with a β source. The observations are in good agreement with the simulated $\sigma_{\text{ionisation}}$ behaviour using Weightfield2 [22].

all timing resolution. Similarly, the mean of extracting the CFD value was compared between interpolating a data point via a linear fit to the two closest sampling points at the 30% threshold recorded by the oscilloscope, and using a spline fit along the rising edge of the signal shape. Again, there was no discernible effect on the timing resolution.

3.2. Intrinsic MCP timing resolution

The MCP timing resolution is computed using the data collected with the EXFLU 20 μm sensors, which give a very similar timing performance to one another. This assumes a tri-plane setup whereby the CFD value at 30% is measured for each pairing of planes, which gives the difference in time of arrival between each DUT and the MCP, as well as the difference between the two DUTs. From these differences, $\sigma_t^2(\text{DUT1; MCP})$, $\sigma_t^2(\text{DUT2; MCP})$, and $\sigma_t^2(\text{DUT1; DUT2})$ are extracted with a Gaussian fit. The value for $\sigma_t(\text{MCP})$ is computed in this case using the equation:

$$\sigma_t(\text{MCP}) = \frac{1}{\sqrt{2}} \sqrt{\sigma_t^2(\text{DUT1; MCP}) + \sigma_t^2(\text{DUT2; MCP}) - \sigma_t^2(\text{DUT1; DUT2})}, \quad (7)$$

where DUT 1 is the 20 μm CHBL sensor of higher operating bias, DUT 2 is the 20 μm CBL sensor of lower operating bias, and the terms above exploit the quadrature relations:

$$\begin{aligned} \sigma_t^2(\text{DUT1; MCP}) &= \sigma_t^2(\text{DUT1}) + \sigma_t^2(\text{MCP}), \\ \sigma_t^2(\text{DUT2; MCP}) &= \sigma_t^2(\text{DUT2}) + \sigma_t^2(\text{MCP}), \\ \sigma_t^2(\text{DUT1; DUT2}) &= \sigma_t^2(\text{DUT1}) + \sigma_t^2(\text{DUT2}). \end{aligned} \quad (8)$$

The $\sigma_t(\text{MCP})$ value is estimated for multiple sets of data, given that DAQ was performed for several bias points, and an average timing resolution of 5 ± 2 ps is achieved.

4. Timing performance from test on a 4 GeV/c electron beam

The timing resolution $\sigma_t(\text{DUT})$ of all non-irradiated EXFLU samples studied at the Test Beam Facility is presented in Figure 13 as a function of the injected charge, with the lowest measured value for timing resolution of each sensor thickness, $\sigma_t(\text{DUT})_{\min}$, given in Table 2. The values for $\sigma_t(\text{DUT})$ use the single-sensor plane method and Equation 6, for a $\sigma_t(\text{MCP})$ of 5 ± 2 ps. The most evident trend is the effect of sensor thickness on

$\sigma_t(\text{DUT})$, corresponding to the linear decrease in t_{rise} with substrate thickness highlighted in Figure 10.

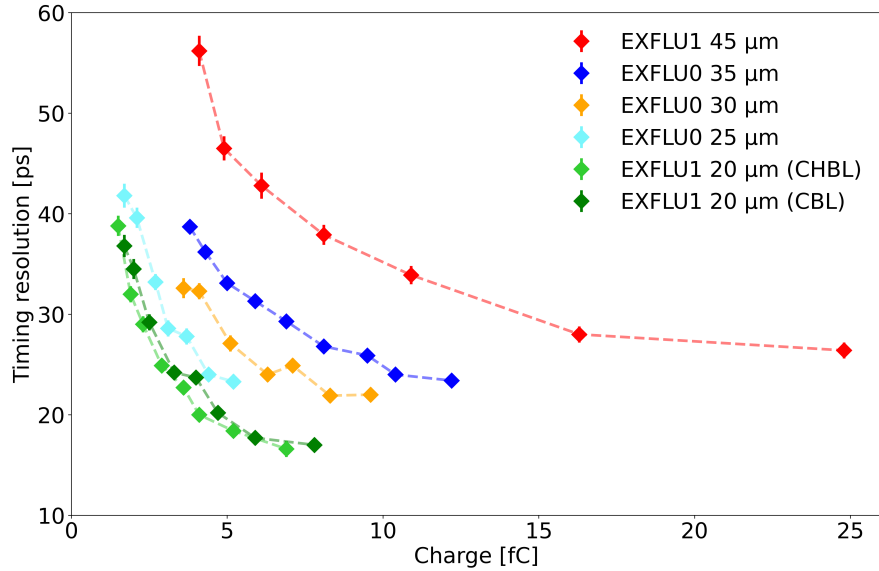


Figure 13: The $\sigma_t(\text{DUT})$ values across all non-irradiated EXFLU samples as a function of the charge injected, illustrating the effect of sensor thickness on timing precision. The 45 μm result is recorded using β -source electrons.

The amount of collected charge necessary to reach a given $\sigma_t(\text{DUT})$ is also observed to decrease linearly with the sensor thickness, illustrated in Figure 14. In this case, the CBL-activated 20 μm device is used as the reference, although the performance of the two 20 μm sensors is nearly identical. The data demonstrate that, for a sub-30 ps $\sigma_t(\text{DUT})$, the minimum collected charge is more than a factor of 2.5 smaller between the 35 μm and 20 μm sensors, decreasing from ~ 6 fC to ~ 2 fC. The corresponding minimum charge for a 45 μm sensor is ~ 15 fC.

The timing resolution of a two-plane LGAD tracker setup using 20 μm DUTs has been evaluated to verify the overall σ_t scaling by a factor of $1/\sqrt{2}$. By treating the time of the track as the average of the times of arrival in each 20 μm DUT, the resulting Gaussian fit yields a $\sigma_t(\text{DUT1}; \text{DUT2})$ of 12.2 ps, once subtracting the $\sigma_t(\text{MCP})$ contribution. The results of the LGAD tracker for the 20 μm samples are shown against collected charge in Figure 15.

In the irradiated samples, a timing resolution of 20 ps is achieved across

Table 2: The lowest measured $\sigma_t(\text{DUT})$ value achieved for each non-irradiated EXFLU sensor thickness.

Thickness [μm]	$\sigma_t(\text{DUT})_{\min}$ [ps]
45	26.4 ± 1.7
35	23.4 ± 0.5
30	22.0 ± 0.7
25	23.3 ± 0.8
20	16.6 ± 0.7

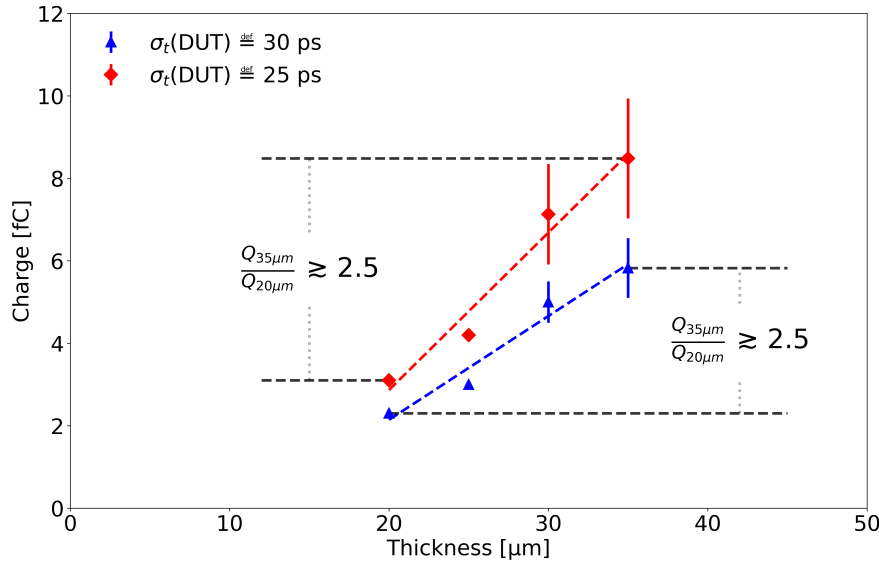


Figure 14: The minimum collected charge required to achieve a fixed $\sigma_t(\text{DUT})$ value as a function of sensor thickness, highlighting the sensitivity between different EXFLU samples for a signal measured with a given precision. The uncertainties in the charge estimates are not shown.

all irradiated sensors except for the $2.5 \times 10^{15} \text{ n}_1 \text{ MeV eq.cm}^{-2}$ sample. The results are shown in Figure 16 as a function of the reverse bias, and in Figure 17 relative to the collected charge using data taken with irradiated samples at temperatures within the range of -50 and -35°C. The non-irradiated 30 μm sample is shown for reference. The results of the $2.5 \times 10^{15} \text{ n}_1 \text{ MeV eq.cm}^{-2}$ indicate that a $\sigma_t(\text{DUT})$ of 20.5 ps is the best achievable before the SEB region [19] is reached. The change in temperature does not affect the $\sigma_t(\text{DUT})$ measurements, and hence no bias correction is applied.

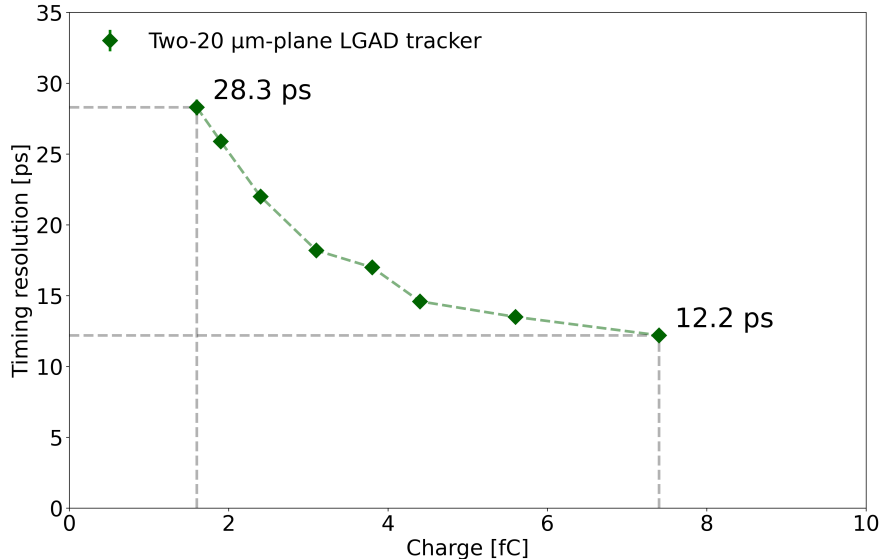


Figure 15: The timing resolution of a two-plane LGAD tracker setup with the 20 μm samples, where the average time of arrival of each DUT is used to compute the value for $\sigma_t(\text{DUT1}; \text{DUT2})$. The lowest $\sigma_t(\text{DUT1}; \text{DUT2})$ achieved by the two-plane tracking system is 12.2 ps.

5. Conclusion

The results of a test on a particle beam using 4 GeV/c electrons at the Test Beam Facility at DESY show that very thin sensors from the EXFLU production with substrate thicknesses below 35 μm can achieve sub-25 ps timing precision, and as good as 16.6 ps in 20 μm sensors. A two-plane LGAD tracker setup using the 20 μm samples achieved a timing resolution

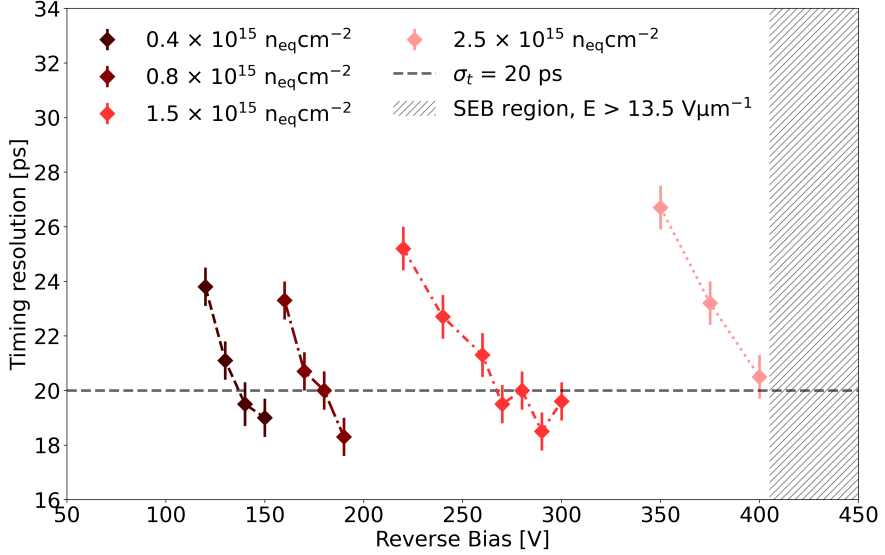


Figure 16: The timing resolution of the 30 μm sensors as a function of reverse bias, using data obtained between -50 and -35°C, with a 20 ps baseline shown for reference.

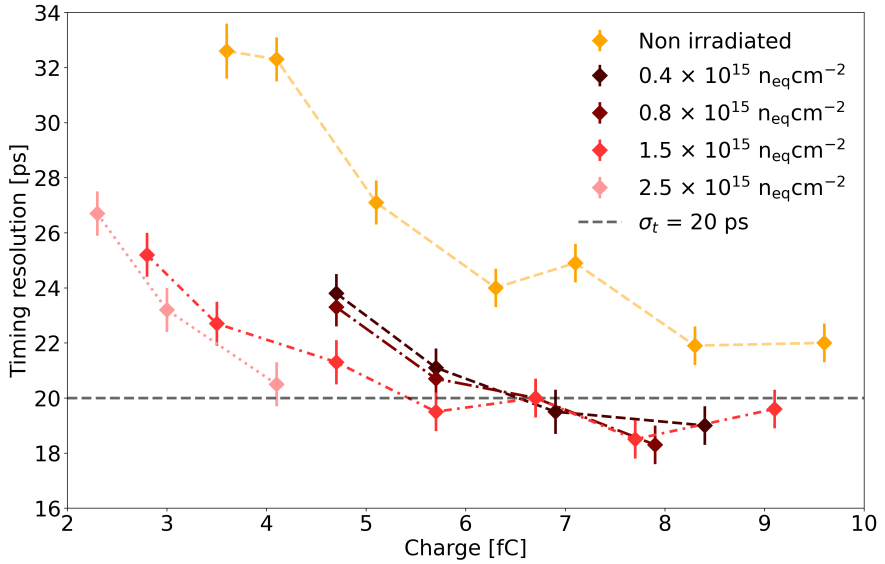


Figure 17: The timing resolution of the 30 μm sensors as a function of collected charge, using data obtained between -50 and -35°C. The non-irradiated sample tested at 18°C is shown for reference.

of 12.2 ps. The improvement with substrate thickness is understood as the signal t_{rise} and $\sigma_{\text{ionisation}}$ are inherently smaller for thinner LGADs.

As expected, for a given gain, the signal amplitude is observed to be independent of the substrate dimensions.

The minimum amount of charge required to achieve a given timing precision is observed to decrease linearly with active thickness. To achieve a sub-30 ps timing resolution, the minimum collected charge is more than a factor of 2.5 smaller between the 35 μm and 20 μm sensors, decreasing from $\sim 6 \text{ fC}$ to $\sim 2 \text{ fC}$.

A study using irradiated 30 μm sensors demonstrated that a timing resolution of 18.3 ps is achieved for sensors irradiated at fluences up to $1.5 \times 10^{15} \text{ n}_1 \text{ MeV}_{\text{eq.}} \text{cm}^{-2}$, and 20.5 ps at $2.5 \times 10^{15} \text{ n}_1 \text{ MeV}_{\text{eq.}} \text{cm}^{-2}$ before reaching the SEB limit.

Acknowledgements

This project has received funding from the European Union’s Horizon 2020 research and innovation programme under Grant Agreements Nos 101004761 (AIDAInnova) and 101057511 (EURO-LABS), the European Union - Next Generation EU, Mission 4 Component 1 CUP D53D23002870001 (Comon-Sens), and the INFN CSN5 through the ‘eXFlu’ research project. The measurements leading to these results have been performed at the Test Beam Facility at DESY, Hamburg (Germany), a member of the Helmholtz Association (HGF).

References

- [1] L. Rossi, O. Brüning, High Luminosity Large Hadron Collider: A description for the European Strategy Preparatory Group, Tech. Rep. 236, CERN, Geneva (2012).
URL <https://cds.cern.ch/record/1471000>
- [2] A. La Rosa, The Upgrade of the CMS Tracker at HL-LHC, JPS Conf. Proc. 34 (2021) 010006. doi:10.7566/JPSCP.34.010006.
- [3] G. Aad, The ATLAS Upgrade for the HL-LHC, CERN (6 2025).

- [4] M. Benedikt, A. Chance, B. Dalena, D. Denisov, M. Giovannozzi, J. Gutleber, R. Losito, M. Mangano, T. Raubenheimer, W. Riegler, V. Shiltsev, D. Schulte, D. Tommasini, F. Zimmermann, Future Circular Hadron Collider FCC-hh: Overview and Status (2022). [arXiv:2203.07804](https://arxiv.org/abs/2203.07804).
- [5] G. Pellegrini, P. Fernández-Martínez, M. Baselga, C. Fleta, D. Flores, V. Greco, S. Hidalgo, I. Mandić, G. Kramberger, D. Quirion, M. Ullan, Technology developments and first measurements of Low Gain Avalanche Detectors (LGAD) for high energy physics applications, *Nucl. Instrum. Meth. A* 765 (2014) 12–16. [doi:10.1016/j.nima.2014.06.008](https://doi.org/10.1016/j.nima.2014.06.008).
- [6] M. Ferrero, A. Altamura, R. Arcidiacono, N. Cartiglia, M. Durando, L. Lanteri, C. Marinuzzi, L. Menzio, F. Siviero, V. Sola, R. White, FAST3 ASIC: an analog front-end with 30 ps resolution, designed to readout thin Low Gain Avalanche Diodes, *Journal of Instrumentation* 20 (03) (2025) C03007. [doi:10.1088/1748-0221/20/03/C03007](https://doi.org/10.1088/1748-0221/20/03/C03007).
- [7] R. Padilla, C. Labitan, Z. Galloway, C. Gee, S. Mazza, F. McKinney-Martinez, H.-W. Sadrozinski, A. Seiden, B. Schumm, M. Wilder, Y. Zhao, H. Ren, Y. Jin, M. Lockerby, V. Cindro, G. Kramberger, I. Mandiz, M. Mikuz, M. Zavrtanik, R. Arcidiacono, N. Cartiglia, M. Ferrero, M. Mandurrino, V. Sola, A. Staiano, Effect of deep gain layer and Carbon infusion on LGAD radiation hardness, *J. Instrum.* 15 (2020) P10003. [doi:10.1088/1748-0221/15/10/P10003](https://doi.org/10.1088/1748-0221/15/10/P10003).
- [8] A. Kolšek, V. Radulović, A. Trkov, L. Snoj, Using TRIGA Mark II research reactor for irradiation with thermal neutrons, *Nuclear Engineering and Design* 283 (2015) 155–161. [doi:10.1016/j.nucengdes.2014.03.012](https://doi.org/10.1016/j.nucengdes.2014.03.012).
- [9] M. Tornago, Performances of the latest FBK UFSD production, *Journal of Physics: Conference Series* 2374 (1) (2022) 012137. [doi:10.1088/1742-6596/2374/1/012137](https://doi.org/10.1088/1742-6596/2374/1/012137).
- [10] V. Sola, Present and future development of thin silicon sensors for extreme fluences, Talk at VCI2022 – The 16th Vienna Conference on Instrumentation, Wien (Austria) (2022).
URL <https://indico.cern.ch/event/1044975/contributions/4663663/>

- [11] V. Sola, M. Boscardin, F. Moscatelli, A. Altamura, R. Arcidiacono, G. Borghi, N. Cartiglia, M. Centis Vignali, T. Croci, M. Durando, F. Fi-corella, A. Fondacci, S. Galletto, G. Gioachin, S. Giordanengo, O. Ham-mad Ali, L. Lanteri, L. Menzio, A. Morozzi, D. Passeri, G. Paternoster, F. Siviero, M. Tornago, R. White, Thin LGAD sensors for 4D tracking in high radiation environments: state of the art and perspectives, *Front. Sens.* 6 (2025) 1648102. doi:10.3389/fsens.2025.1648102.
- [12] A. Altamura, R. White, M. Ferrero, L. Anderlini, R. Arcidiacono, G. Borghi, M. Boscardin, N. Cartiglia, M. C. Vignali, T. Croci, F. Davolio, M. Durando, A. Fondacci, S. Galletto, L. Lanteri, L. Menzio, A. Morozzi, D. Passeri, N. Pastrone, F. Siviero, F. Moscatelli, G. Paternoster, V. Sola, Radiation-resistant thin LGADs for enhanced 4D tracking, *Nucl. Instrum. Meth. A* 1081 (2025) 170799. doi:10.1016/j.nima.2025.170799.
- [13] R. Diener, J. Dreyling-Eschweiler, H. Ehrlichmann, I. Gregor, U. Kötz, U. Krämer, N. Meyners, N. Potylitsina-Kube, A. Schütz, P. Schütze, M. Stanitzki, The DESY II test beam facility, *Nucl. Instrum. Meth. A* 922 (2019) 265–286. doi:10.1016/j.nima.2018.11.133.
- [14] R. S. White, R. Arcidiacono, G. Borghi, M. Boscardin, N. Cartiglia, M. C. Vignali, M. Costa, T. Croci, M. Ferrero, A. Fondacci, S. Giordanengo, C. Hanna, L. Lanteri, L. Menzio, A. Morozzi, F. Moscatelli, R. Mulargia, D. Passeri, N. Pastrone, G. Paternoster, V. Sola, Char-acterisation of the FBK EXFLU1 thin sensors with gain in a high flu-ence environment, *Nucl. Instrum. Meth. A* 1068 (2024) 169798. doi: 10.1016/j.nima.2024.169798.
- [15] M. Moll, Acceptor removal - Displacement damage effects involving the shallow acceptor doping of p-type silicon devices, *PoS Vertex2019* (2020) 027. doi:10.22323/1.373.0027.
- [16] M. Ferrero, R. Arcidiacono, M. Mandurrino, V. Sola, N. Cartiglia, An Introduction to Ultra-Fast Silicon Detectors, CRC Press, 2021. doi: 10.1201/9781003131946.
- [17] G. Kramberger, V. Cindro, A. Howard, Z. Kljun, I. Mandic, M. Mikuz, Annealing effects on operation of thin Low Gain Avalanche Detectors, *J. Instrum.* 15 (2020) P08017. doi:10.1088/1748-0221/15/08/P08017.

- [18] F. Siviero, et al., Optimization of the gain layer design of ultra-fast silicon detectors, *Nucl. Instrum. Meth. A* 1033 (2022) 166739. [arXiv: 2112.00561](https://arxiv.org/abs/2112.00561), [doi:10.1016/j.nima.2022.166739](https://doi.org/10.1016/j.nima.2022.166739).
- [19] M. Ferrero, R. Arcidiacono, N. Cartiglia, L. Lanteri, L. Menzio, A. Morozzi, F. Moscatelli, R. Mulargia, F. Siviero, R. White, V. Sola, First study of single-event burnout in very-thin planar silicon sensors, *Front. Phys.* 13 (2025) 1575672. [doi:10.3389/fphy.2025.1575672](https://doi.org/10.3389/fphy.2025.1575672).
- [20] S. Meroli, D. Passeri, L. Servoli, Energy loss measurement for charged particles in very thin silicon layers, *J. Instrum.* 6 (2011) P06013. [doi:10.1088/1748-0221/6/06/P06013](https://doi.org/10.1088/1748-0221/6/06/P06013).
- [21] N. Cartiglia, et al., Design optimization of ultra-fast silicon detectors, *Nucl. Instrum. Meth. A* 796 (2015) 141–148. [doi:10.1016/j.nima.2015.04.025](https://doi.org/10.1016/j.nima.2015.04.025).
- [22] F. Cenna, N. Cartiglia, M. Friedl, B. Kolbinger, H. F. W. Sadrozinski, A. Seiden, A. Zatserklyaniy, A. Zatserklyaniy, Weightfield2: A fast simulator for silicon and diamond solid state detector, *Nucl. Instrum. Meth. A* 796 (2015) 149–153. [doi:10.1016/j.nima.2015.04.015](https://doi.org/10.1016/j.nima.2015.04.015).